



TECHNICAL ARTICLE

# Microstructure Evolution and Mechanical Properties of Inconel 625 Foils

Fangjun Wang, Haiding Liu, Jia Li, Hong Wan, Lichuan Yu, and Binbin Liu

Submitted: 18 February 2022 / Revised: 13 February 2023 / Accepted: 11 March 2023 / Published online: 28 March 2023

The microstructure evolution and mechanical properties of cold-rolled Inconel 625 foil with thickness of 50  $\mu\text{m}$  were investigated. After annealing at 650 and 700  $^{\circ}\text{C}$ , the cold-rolled microstructure transformed into smaller recrystallization grain and annealing twins, while the fraction and particle size of MC carbides increased with increasing aging temperature and duration. TEM analysis confirms the precipitation of irregular lens and near spherical-shaped  $\gamma''$  phase at 700  $^{\circ}\text{C}$ , which is not observed in the sample annealed at 650  $^{\circ}\text{C}$ . The foil after annealing at 650  $^{\circ}\text{C}$  for 48 h exhibits the best mechanical properties with ultimate tensile strength and yield strength of 1515 and 1077 MPa as well as reasonable elongation of 19.5%. But the much larger and coarser carbides result in obvious reduction in tensile properties for the sample after 48 h-aging at 700  $^{\circ}\text{C}$ .

**Keywords** foils, Inconel 625, mechanical properties, recrystallization

## 1. Introduction

The safe operation of nuclear power station is an extremely important issue that has received widespread attention. Nuclear reactors present a harsh environment for component service regardless of the type of reactor. The components in a reactor core tolerate exposure to the coolant, stress, vibration, an intense field of high energy neutrons, or gradients in temperature (Ref 1). Degradation of materials can lead to reduced performance, and in some cases, sudden failure. Therefore, how to monitor the pressure within the reactor vessel accurately and reliably is critical for the safe operation. Metallic foils with thickness of several micrometers are always used as the diaphragm material in the pressure sensor of nuclear power station. For instance, the 316L stainless steel foil is a promising candidate for such application due to its high strength and good corrosion resistance (Ref 2–4). This material can be used in the

pressurized water reactor with coolant temperature below 350  $^{\circ}\text{C}$ , but can hardly meet the requirement in the sodium fast reactor or supercritical water-cooled reactor with higher temperature (Ref 1).

Due to high strength and excellent corrosion resistance at elevated temperatures, Inconel 625 alloy is widely utilized in many fields including aeronautical industry, automotive transportation, and chemical processing (Ref 5, 6). Inconel 625 alloy was originally designed as a solid-solution strengthened alloy with relatively high levels of Cr, Fe, Mo and Nb, in which Cr and Mo were added for corrosion resistance, Fe reduced cost, while Nb acted as a solid-solution strengthener (Ref 7, 8). From this aspect, it seems that the Inconel 625 alloy acts as a potential candidate for the usage of pressure sensor. However, some ordered phases would precipitate at elevated temperature. The  $\gamma''$  phase with body-centered tetragonal  $\text{DO}_{22}$  structure forms after annealing at temperatures from 550 to 750  $^{\circ}\text{C}$  (Ref 9), which further transforms into the brittle  $\delta$  phase at higher temperature (Ref 10). Such transformation has great impact on both room- and high-temperature mechanical properties (Ref 11–13). Meanwhile, there are also various carbides precipitated in the matrix, such as MC ('M' rich in Nb, and Ti),  $\text{M}_{23}\text{C}_6$  ('M' rich in Cr),  $\text{M}_6\text{C}$  ('M' rich in Ni, Nb and Mo) (Ref 14), which affects the toughness and ductility of Inconel 625 alloy as well (Ref 15). These carbides can further decompose into the brittle TCP phases and act as crack nucleation sites during creep tests at 850  $^{\circ}\text{C}$  (Ref 16).

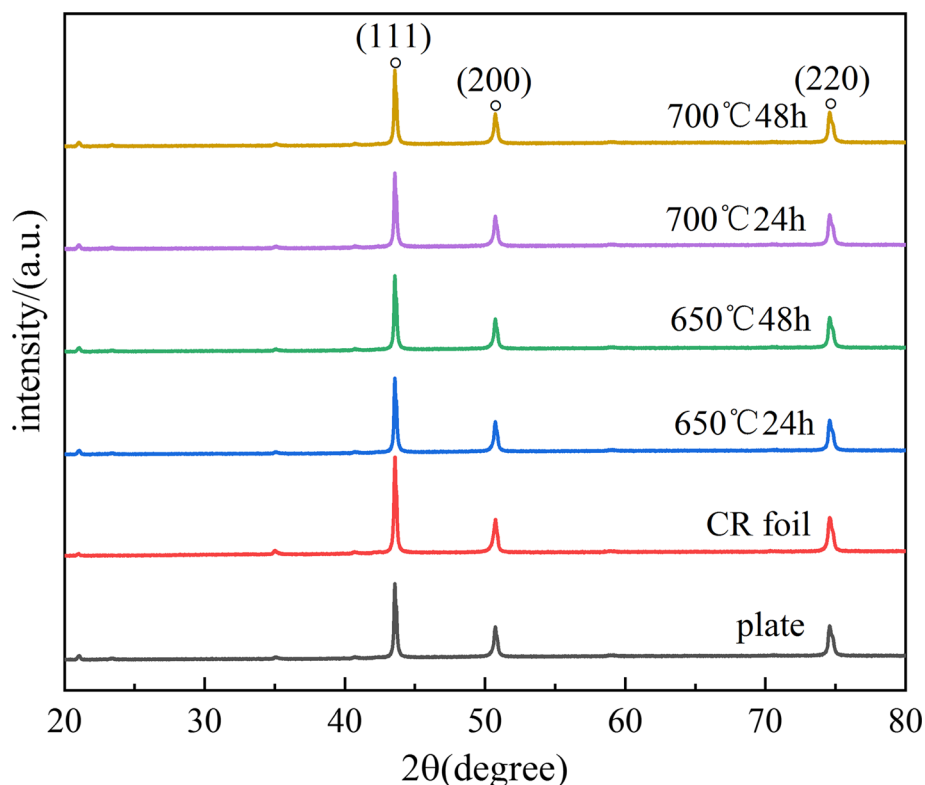
Although the microstructure evolution and its influence on the mechanical properties has been widely investigated (Ref 17–20), seldom studies were performed in the Inconel 625 foil. Therefore, the Inconel 625 foil with 158 mm in width and 50  $\mu\text{m}$  in height was fabricated through multiple rolling process. The coolant inlet and outlet temperature for the supercritical water-cooled reactor and sodium-cooled fast reactor are below 600  $^{\circ}\text{C}$ , while those for the lead-cooled fast reactor range from 600 to 800  $^{\circ}\text{C}$  (Ref 1). Hence, the annealing temperature was set to be 650 and 700  $^{\circ}\text{C}$  to study the effect of shorter time exposure on microstructure and mechanical properties, which will serve as a guideline for the application

**Supplementary Information** The online version contains supplementary material available at <https://doi.org/10.1007/s11665-023-08114-x>.

**Fangjun Wang, Haiding Liu, and Hong Wan**, Chongqing Materials Research Institute Co., Ltd., Chongqing 400707, China; and National Instrument Functional Materials Engineering, Chongqing 400707, China; **Jia Li**, State Key Laboratory for Advanced Metals and Materials, University of Science and Technology Beijing, 30 Xueyuan Road, Beijing 100083, China; **Lichuan Yu**, Chongqing Silian Measurement and Control Technology Co. Ltd., Chongqing 401121, China; and **Binbin Liu**, State Key Laboratory for Advanced Metals and Materials, University of Science and Technology Beijing, 30 Xueyuan Road, Beijing 100083, China; and Institute of Materials Physics, University of Muenster, 48149 Muenster, Germany. Contact e-mail: bblu@ustb.edu.cn.

**Table 1** The chemical composition of Inconel 625 alloy foil (in wt.%)

C	Si	Mn	P	Cr	Mo	Nb	Fe	Co	Ti	Al	Ni
0.036	0.044	0.19	0.0016	21.61	8.53	3.86	2.21	0.015	0.18	0.24	Bal

**Fig. 1** XRD patterns of the Inconel 625 plate and cold-rolled foils with various states

of pressure sensor in the new-generation nuclear power station. The results indicated that the foil after annealing at 650 °C for 48 h exhibits the best mechanical properties with highest ultimate tensile strength and yield strength. The much larger and coarser carbides result in obvious reduction in tensile properties for the sample after 48 h-aging at 700 °C. This result suggests that the Inconel 625 foil is not suitable for long-time usage at the temperature of 700 °C and above.

## 2. Experimental Details

The Inconel 625 alloy ingot with a diameter of 400 mm and a total weight of 1 ton was produced by vacuum induction melting followed by electroslag re-melting. After forging, the ingot was then hot rolled to the plate with thickness of 2.5 mm, which was finally cold rolled to foil with 158 mm in width and 50  $\mu\text{m}$  in height. The obtained foil was heated to 1000 °C for 3 min to eliminate processing stress. The nominal chemical compositions of Inconel 625 alloy foil are listed in Table 1. The impurity elements with content below 0.001% such as S and B are hardly determined. With respect to the serviceability temperature of foils used as pressure sensor, the samples were annealed at 650 and 700 °C for 2 and 48 h

followed by furnace cooling to room temperature to study microstructure evolution and mechanical properties. Here, the properties of the thicker plate and foil without heating treatment are also shown for comparison.

Phase composition was examined by x-ray diffraction using Cu  $K\alpha$  radiation in a Rigaku TTR III x-ray diffractometer (XRD). Microstructure of both the alloy plate and foils with various states were characterized in the Zeiss ImageA2M optical microscope (OM) and Zeiss Super<sup>55</sup> scanning electron microscope (SEM) equipped with combined EDS/WDS (energy-dispersive spectrometer/wavelength-dispersive spectroscopy). Small areas with size of  $1 \times 1 \mu\text{m}$  were selected for EDS/WDS analyses, so as to avoid large deviation in determining compositions. Pure Fe and Cu are introduced for calibration before EDS/WDS tests. Before OM tests, the samples were ground, mechanically polished using a 1- $\mu\text{m}$  diamond paste and then, etched in aqua regia. Electron backscatter diffraction (EBSD) was performed in the FEI Nano Nova SEM 230. The preparation of EBSD samples follows the below sequence: mechanical grinding using abrasive SiC papers (SiC paper with particle diameter of 6.5  $\mu\text{m}$  for 5 s + SiC paper with particle diameter of 5  $\mu\text{m}$  for about 30 s), mechanical polishing by 3  $\mu\text{m}$  diamond suspensions for 1–2 min, and followed by a final step with oxide polishing

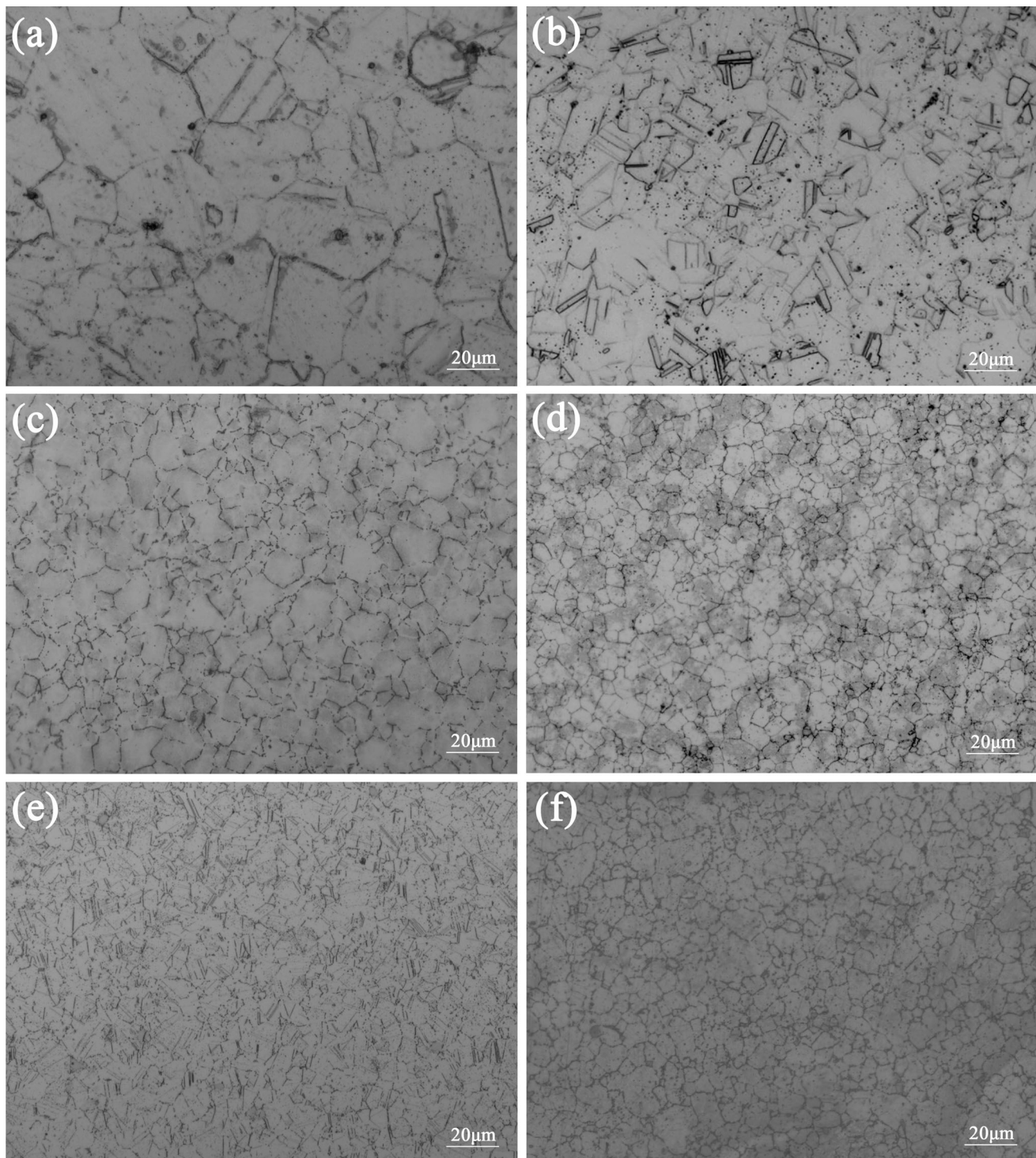


**Fig. 2** Typical OM images of Inconel 625 alloy: (a) plate, (b) CR foil, (c) 650 °C for 24 h, (d) 650 °C for 48 h, (e) 700 °C for 24 h, (f) 700 °C for 48 h

suspension (OPS). Transmission electron microscopy (TEM) studies were performed in a Tecnai G2 F30. The sliced specimens in the shape of 3-mm-diameter disks for TEM observation were grinded and thinned using a twin-jet technique in the electrolyte of 10% HClO<sub>4</sub> and 90% ethanol solution.

Tensile experiments were performed in the Instron5969 foil testing machine at a nominal strain rate of  $1 \times 10^{-3} \text{ s}^{-1}$ . The tensile tests were performed three times for each state. In order

to avoid warping, the foil with length of 120 mm along the rolling direction was placed between two thin stainless-steel plates with the same size to form the steel/Inconel625 foil/steel sandwich structure. Then, the bone-shaped tensile samples with gauge length of 24 mm and width of 8 mm were cut from the sandwich structure through wire electrical discharge machining. The total length and width for the tensile sample are 100 and 30 mm, respectively. The serrated jaw faces with a surface area large enough to cover as much surface of the sample's grip

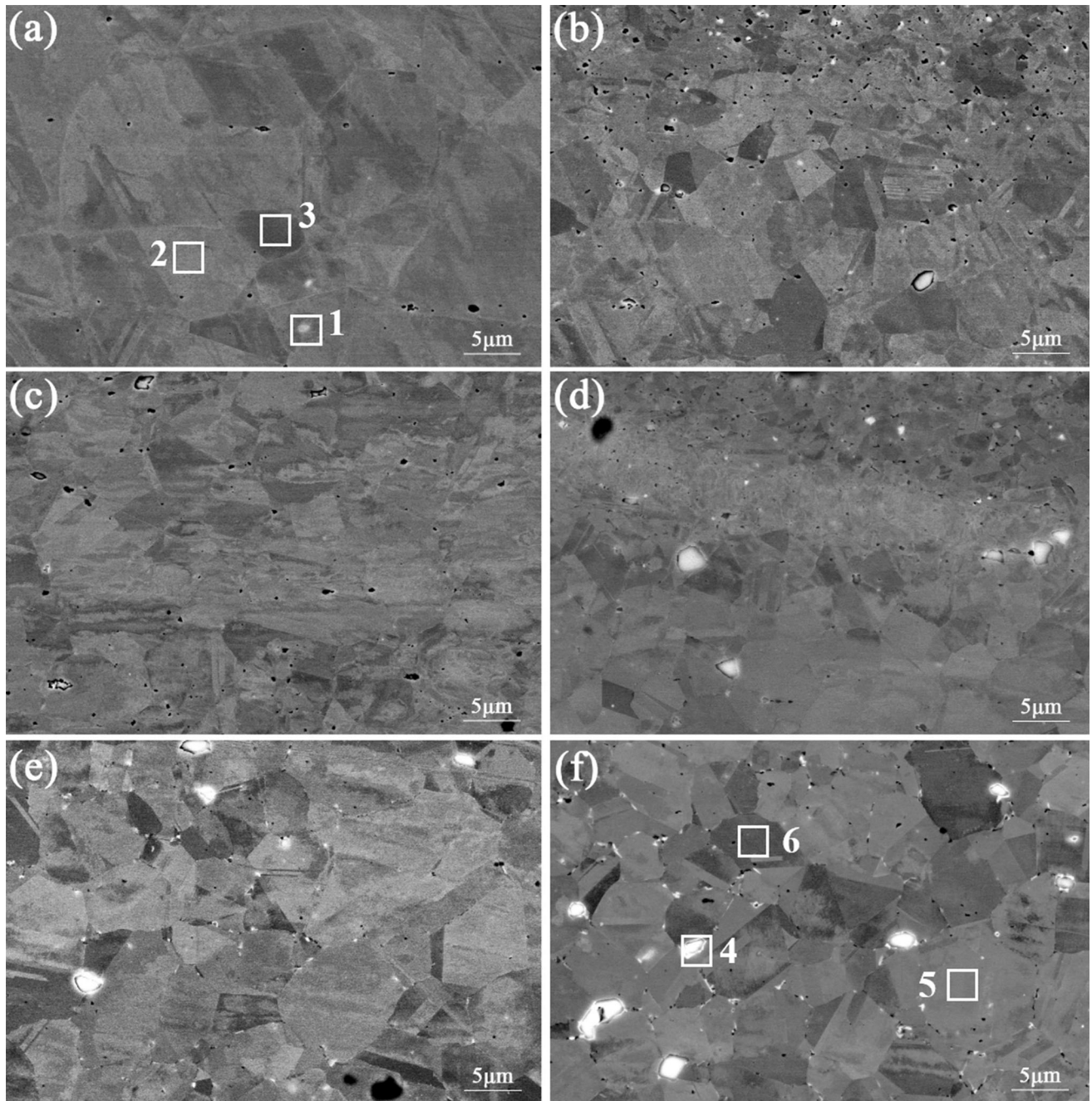


**Fig. 3** Typical SEM images of Inconel 625 alloy: (a) plate, (b) CR foil, (c) 650 °C for 24 h, (d) 650 °C for 48 h, (e) 700 °C for 24 h, (f) 700 °C for 48 h

**Table 2** Compositions in wt.% of the CR Inconel 625 foil and the sample after annealed at 700 °C for 48 h

Areas	C	Ti	Cr	Mn	Fe	Al	Nb	Mo	Ni
1	0.83 ± 0.01	1.31 ± 0.02	16.82 ± 0.05	...	1.69 ± 0.03	0.42 ± 0.02	28.03 ± 0.1	4.01 ± 0.06	46.65 ± 0.11
2	0.44 ± 0.01	0.20 ± 0.02	22.78 ± 0.06	0.20 ± 0.04	2.03 ± 0.03	0.02 ± 0.01	4.47 ± 0.08	9.01 ± 0.08	60.82 ± 0.12
3	0.46 ± 0.01	0.24 ± 0.02	22.98 ± 0.06	0.23 ± 0.04	2.17 ± 0.03	0.02 ± 0.01	4.31 ± 0.09	8.53 ± 0.08	61.02 ± 0.12
4	1.46 ± 0.04	1.06 ± 0.02	17.85 ± 0.05	...	1.91 ± 0.04	0.4 ± 0.02	31.59 ± 0.11	...	45.48 ± 0.11
5	0.43 ± 0.01	0.13 ± 0.02	23.07 ± 0.05	0.25 ± 0.02	2.75 ± 0.04	0.1 ± 0.02	4.07 ± 0.09	8.64 ± 0.08	60.54 ± 0.09
6	0.44 ± 0.01	0.16 ± 0.02	23.26 ± 0.05	0.10 ± 0.02	2.71 ± 0.03	0.01 ± 0.01	4.04 ± 0.09	8.73 ± 0.09	60.55 ± 0.09

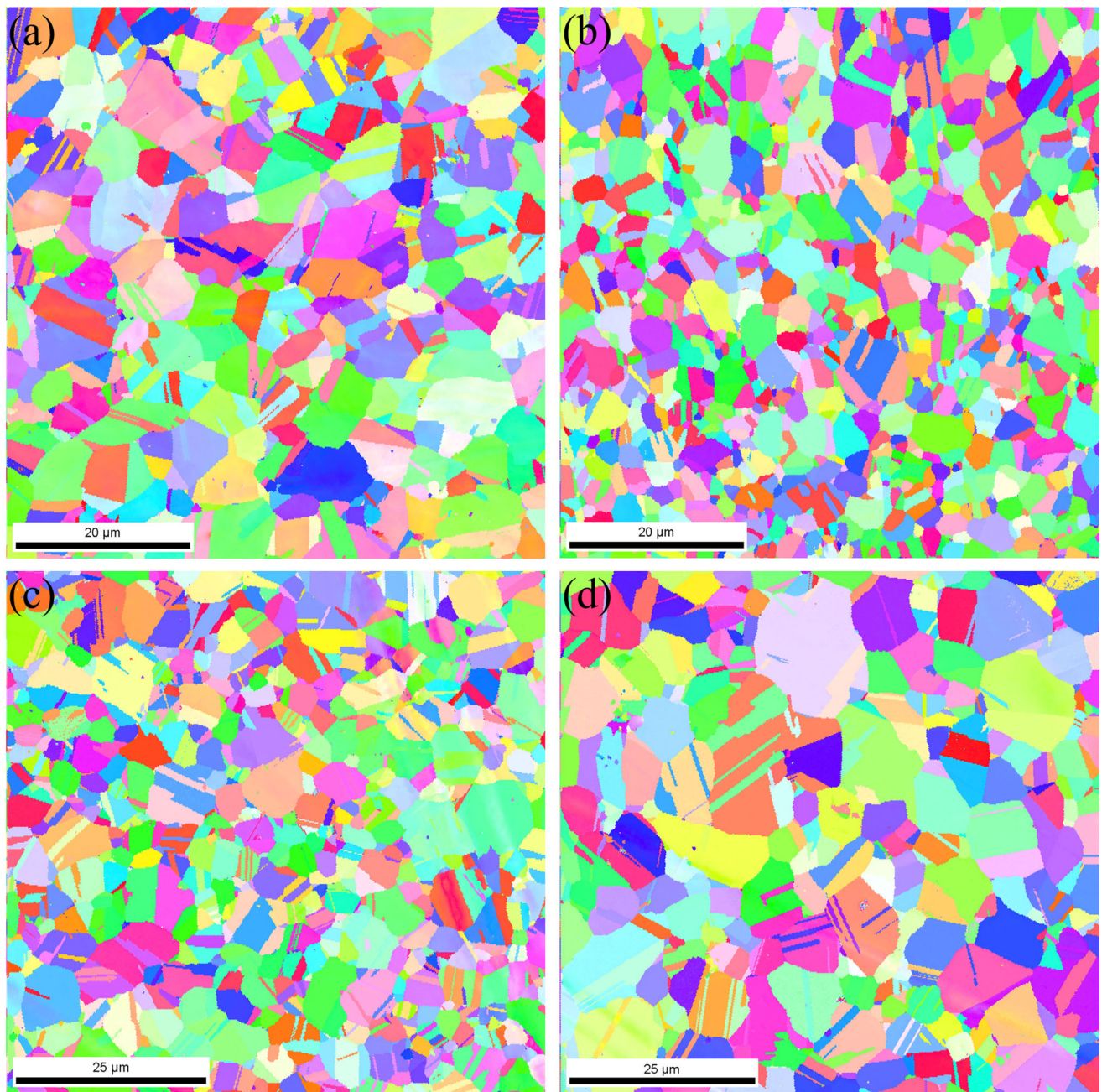


**Fig. 4** EBSD images for the annealed Inconel 625 foils: (a) 650 °C for 24 h, (b) 650 °C for 48 h, (c) 700 °C for 24 h, (d) 700 °C for 48 h

section as possible are used to grip the tensile sample. Typically, the specimen is gripped by at least 75% of the available jaw face length. Before each test, the crosshead is moved to its starting position and the zero-extension point is calibrated. The self-aligning coupling adapters are used to adjust the direction of the test load, which helps to minimize possible bending load on the foil. Tensile fracture morphology for foils was also observed in SEM.

### 3. Results

Figure 1 shows the XRD patterns of the Inconel 625 plate and foils with different states. The CR foil represents the cold-rolled foil followed by stress-relief annealing. Other than those

strong diffraction peaks belonging to the face centered cubic (FCC) austenite matrix, some weak peaks of carbides are observed in all the samples.

Microstructure evolution of Inconel 625 alloy at different states was further studied. The alloy plate shows typical deformation microstructure with a mixture of extensively serrated and bulging grains accompanied by some deformation twins as seen in the OM images in Fig. 2(a). SEM image in Fig. 3(a) further suggests that few white tiny particles marked as Area-1 randomly distribute in both grain interiors and grain boundary, which was found enriching in C, Nb and Ti but depleting in Cr, Ni and Fe as verified by EDS/WDS results in Table 2, while Area-2 and 3 individually selected from the gray and dark regions of the matrix have closed composition. Here, it should be stressed that it is difficult to obtain the actual

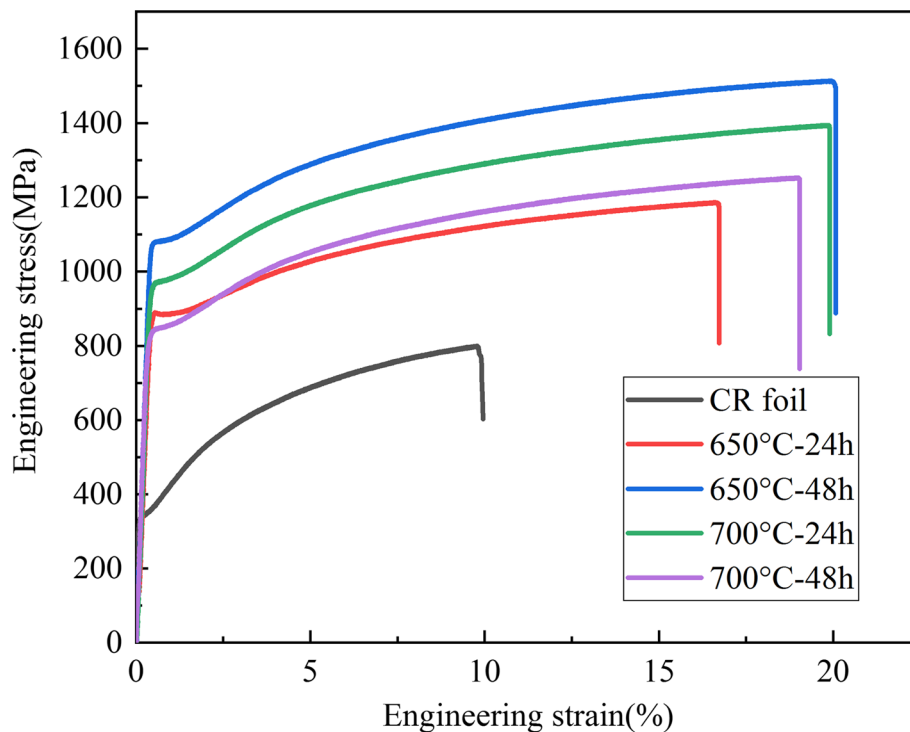


**Fig. 5** The stress–strain curves of the Inconel 625 CR foil and foils after annealed at 650 and 700 °C for 24 and 48 h

**Table 3** Ultimate tensile strength (UTS), yield strength (YS), elongation of Inconel 625 foil in different states

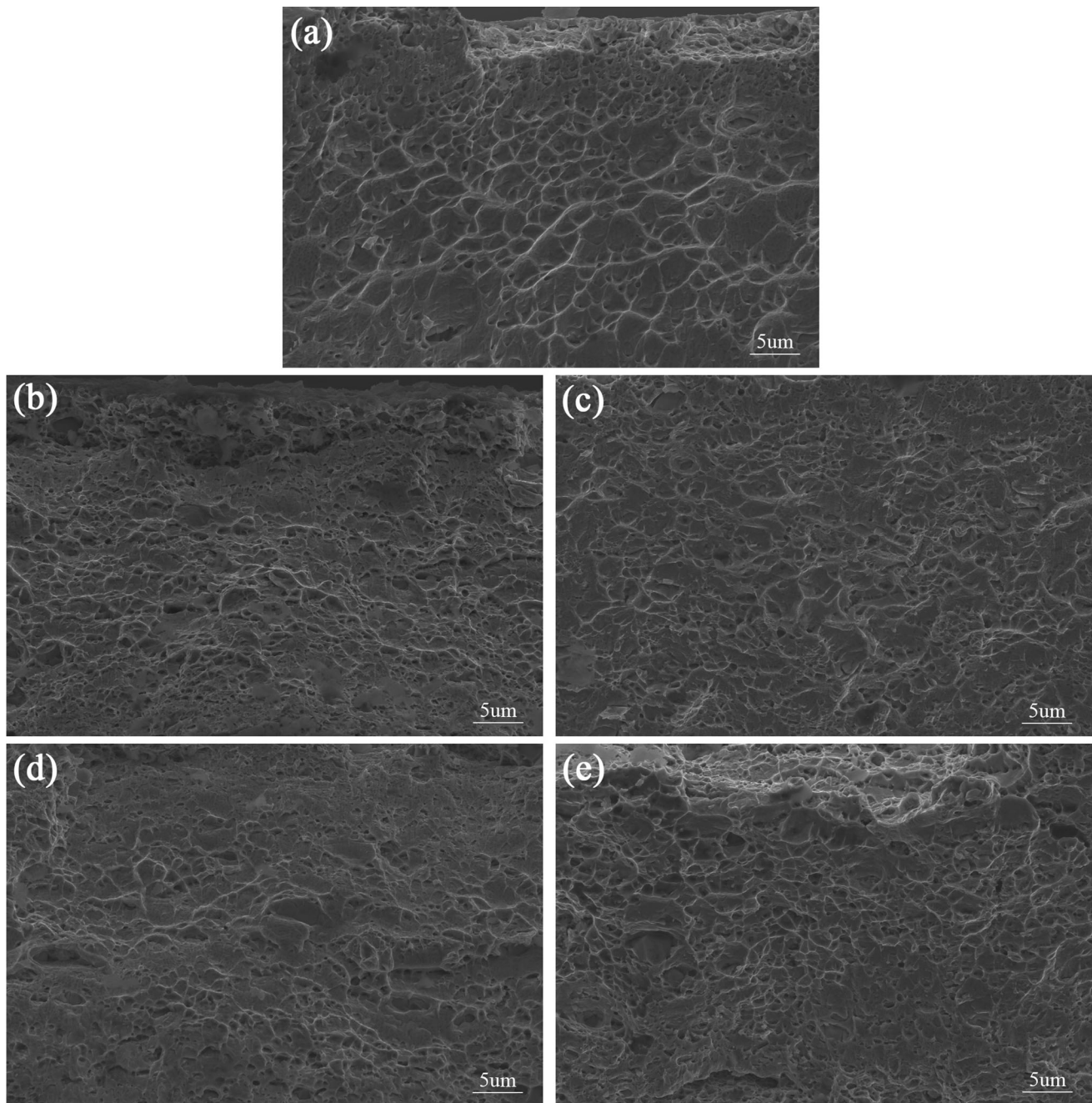
Samples	UTS, MPa	YS, MPa	Elongation, %
CR foil	800	340	~ 9.5
650 °C-24 h	1185	888	~ 16.5
650 °C-48 h	1513	1077	~ 19.5
700 °C-24 h	1394	969	~ 19.4
700 °C-48 h	1250	846	~ 18.5

content of light elements such as carbon only through EDS/WDS analysis, obtained values listed in Table 2 are used for reasonable comparison. Much smaller grains together with more twins were observed in the CR foil (Fig. 2b). More tiny carbides embedded in the matrix, which easily fell off during sample preparation, are indicated by small holes in Fig. 3b. It should be noted that the fine carbides tend to aggregate to form larger particles with size of 2  $\mu\text{m}$ . After annealed at 650 °C for 24 and 48 h, the deformation morphology has changed to be equiaxed grains as well as some annealing twins, indicating the occurrence of recrystallization as shown in OM images in Fig. 2(c–d) and SEM images in Fig. 3(c–d), which is clearly observed in the EBSD images in Fig. 4(a–b). The grain size for the sample after annealed at 650 °C for 24 h mainly ranges from 2 to 8  $\mu\text{m}$  as calculated by OIM Analysis™ software based on the EBSD image (seeing supplementary Fig. S1a). However, some small grains were observed in the sample after annealed at 650 °C for 48 h, although the grain size is still from 2 to 8  $\mu\text{m}$  (Fig. 4b and Fig. S1b). Generally, the recrystallized grain size would increase with the annealing time. This result implies that recrystallization did not happen homogeneously throughout the whole foil, which is consistent with the

observation of partial recrystallization region in SEM image (Fig. 3d). As shown in Fig. 3d, these grains adjacent to the partial recrystallization region have smaller grain size. Indeed, in addition to the deformation degree, other factors such as original grain size and second phase particles affect the recrystallization behavior as well.

Similar phenomenon is also observed in the samples after annealing at 700 °C in Fig. 2(e–f) and 3(e–f). The EBSD image in Fig. 4(c) implies that, after annealing at 700 °C for 24 h, the grain size of the annealed sample mainly ranges from 2 to 8  $\mu\text{m}$  as well, but a small number of grains with size from 8 to 9  $\mu\text{m}$  were observed. When the annealing time reached 48 h, some equiaxed grains with size larger than 10  $\mu\text{m}$  formed (Fig. 4d and S1d), which might be attributed to the quick migration of recrystallization grain boundaries at higher temperature. Meanwhile, the fraction and particle size of carbides increased as annealing temperature and times increased. Particularly, some much larger carbides with size exceeding 7  $\mu\text{m}$  were clearly observed in the foil after 48 h-annealed at 700 °C. EDS/WDS is again performed to compare the composition of the carbides and the matrix as listed in Table 2. It can be found that the carbide particle in Area-4 still enriches in C, Nb and Ti in comparison with the matrix (Area-5 and Area-6), and the content of C and Nb is higher than that of the CR foil without annealing.

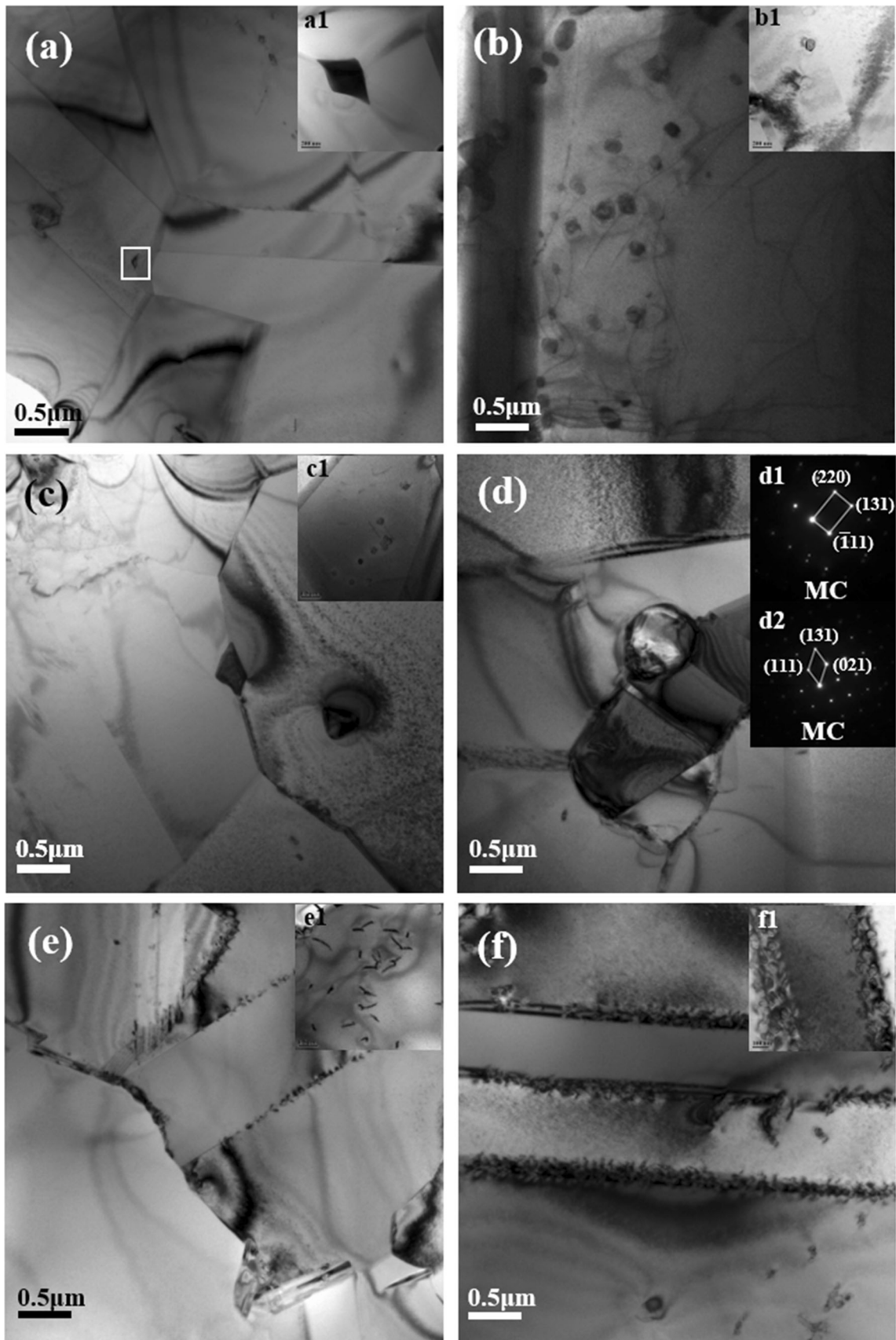
The mechanical properties of the CR foil and those samples after heat treatment are further compared. Figure 5 presents the tensile stress–strain curves of the Inconel 625 with different states. The ultimate tensile strength (UTS), yield stress (YS) and elongation for the CR foil are 800 MPa, 340 MPa and 9.5%, respectively. A remarkable increase in both strength and ductility was achieved in those foils after heating treatment as seen in Fig. 5 and listed in Table 3. The UTS and YS increase to 1185 and 888 MPa after annealing at 650 °C for 24 h, which



**Fig. 6** Typical SEM images of fracture morphology for Inconel 625 alloy: (a) CR foil, (b) 650 °C for 24 h, (c) 650 °C for 48 h, (d) 700 °C for 24 h, (e) 700 °C for 48 h

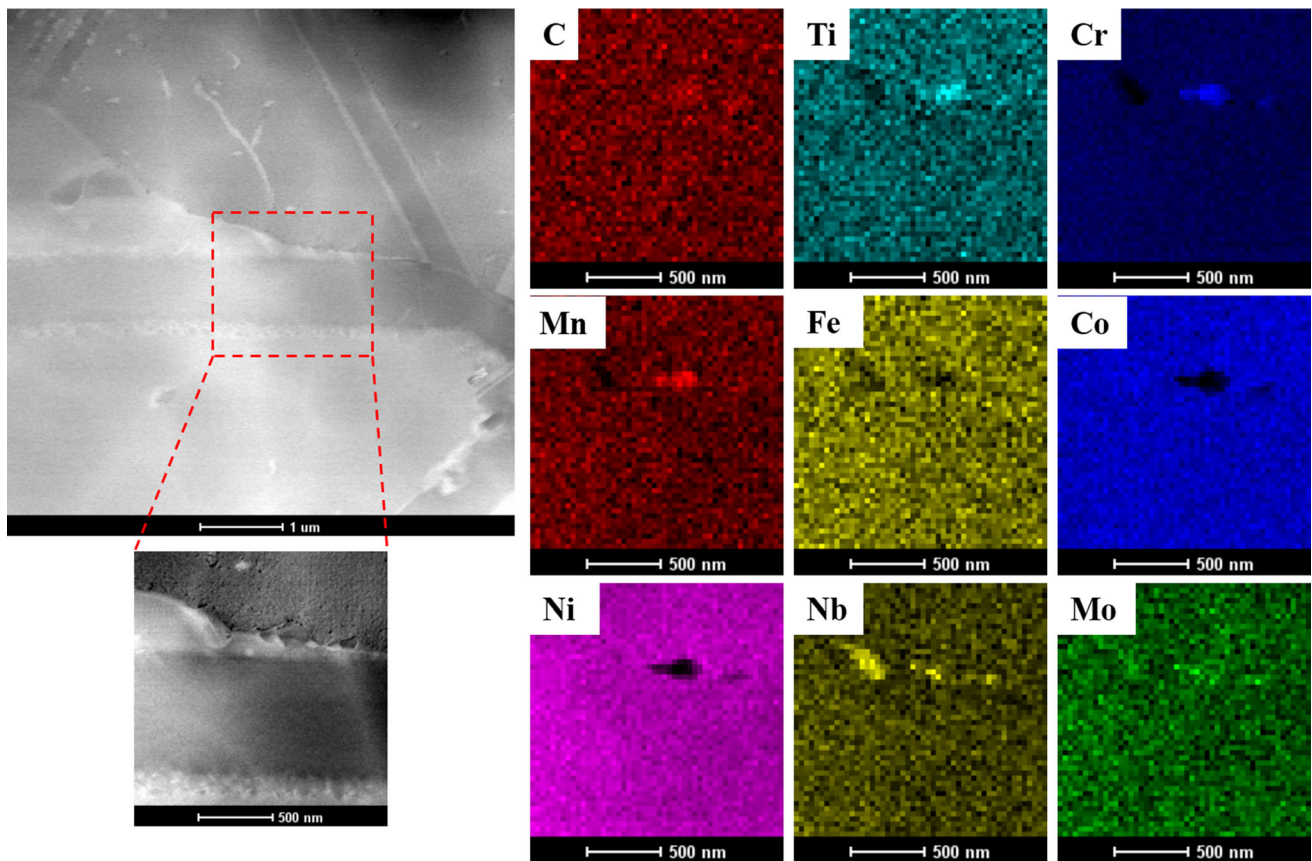
further individually increase to 1513 and 1077 MPa as annealing time extends to 48 h. The dramatic increment of ductility is observed as well. The elongation of 19.4% for the foil after 24 h-annealed at 700 °C is close to that for the sample when treated at 650 °C for 48 h, but both UTS and YS show an obvious decrease. In case of the specimen after annealed at 700 °C for 48 h, a much severe decline of strength and ductility was observed. Here, it should be emphasized that although the ductility of foils is lower than that of casted or forged Inconel 625 alloy with elongation beyond 50%, reasonable values of elongation are still retained for foils with different states, which is confirmed by the fracture morphology as shown in Fig. 6.

Figure 6 illustrates the fracture morphology of Inconel 625 foil with different states. All samples exhibit the appearance of ductile fracture with majority of dimples, indicating a dimpled ductile mode of failure associated with good tensile properties. As comparison with the CR foil, the dimples in the annealed samples become much smaller and deeper. Particularly, the size and the distribution of dimples are more uniform throughout the whole fracture surface of the foil after 48 h annealing at 650 °C, which explains the best mechanical properties for this sample as shown in Fig. 5. In order to gain better understanding of microstructure evolution and mechanical properties, TEM analysis is performed in the CR foil and samples after annealing at 650 and 700 °C for 48 h.



**Fig. 7** TEM images together with the selected area electron diffraction patterns for Inconel 625 alloy: (a–b) CR foil, (c–d) 650 °C for 48 h and (e–f) 700 °C for 48 h





**Fig. 8** EDS elements mapping for the Inconel 625 foil after annealed at 700 °C for 48 h

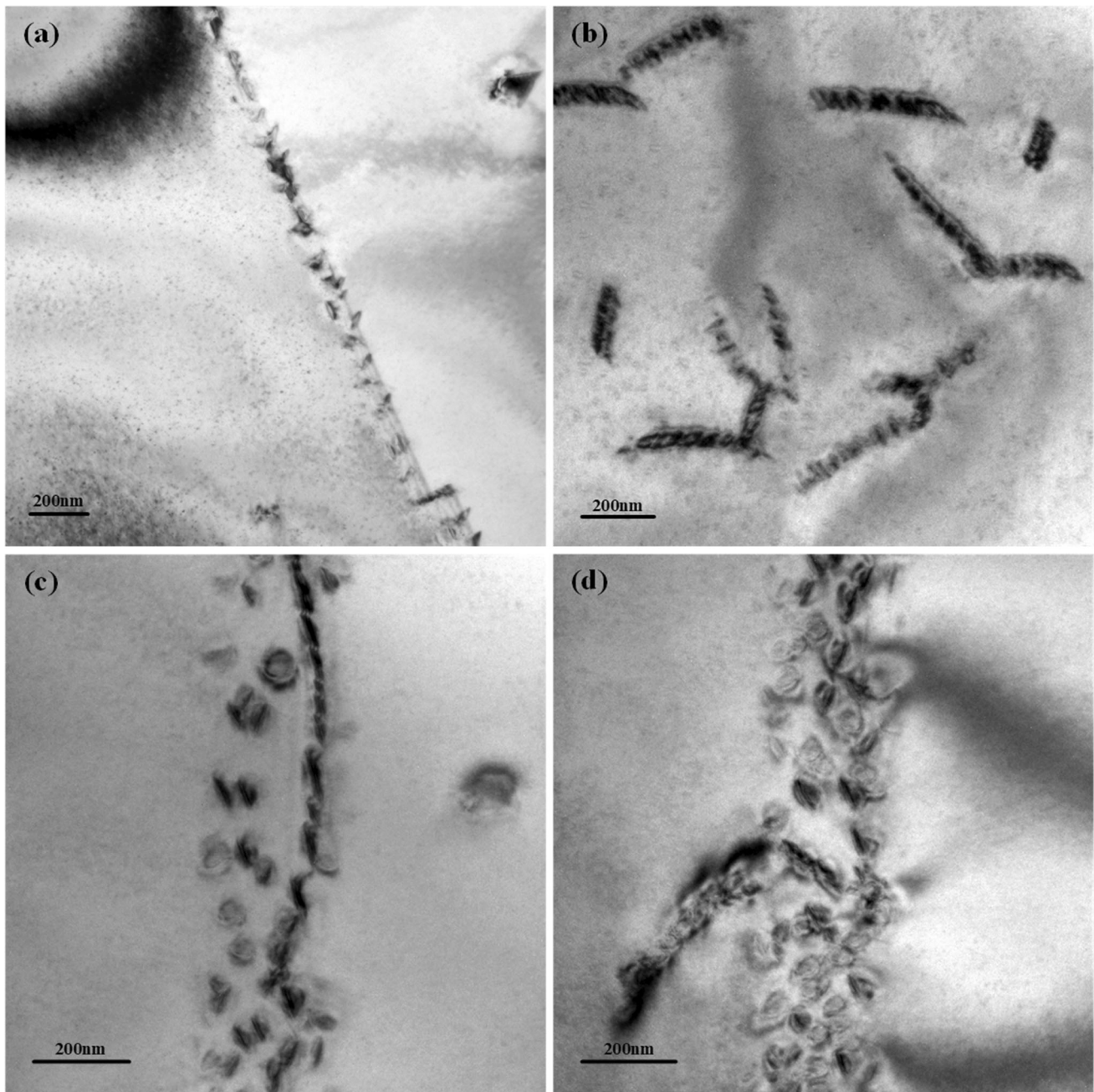
Figure 7(a–b) exhibits the TEM image of Inconel 625 CR foil. Large grain size together with twins could be found. The insert figure in Fig. 7(a) clearly shows the existence of polygonal carbide with size larger than 400 nm in the grain boundary. There are many irregular-shaped precipitations embedded in both grains and twins, which act as barrier for the motion of dislocations (Fig. 7b). As for the foil after 48 h annealing at 650 °C, those irregular-shaped carbides could still be observed in the grain boundary as well as grain interiors as shown in Fig. 7(c) and insert figure. Whereas, the particle size is apparently larger than that in CR foil as seen in Fig. 7(d). The insert two figures (Fig. 7d1–d2) present the selected area electron diffraction patterns (SADPs) of carbides from the grain boundary and inside grain, respectively. The SADP was taken from a region with a diameter of 200 nm. Both SADPs are indexed to be MC carbide, coinciding with the XRD results and EDS/WDS results in Fig. 1 and Table 2. When the annealing temperature increased to 700 °C, some large annealing twins could be found in the foil, while many linear precipitations distribute inside the recrystallization grains as shown in the insert of Fig. 7(e). Apart from these precipitations, plenty of smaller particles formed along the annealing twin boundaries, some of which further grow into annealing twins in favorable locations as seen in Fig. 7(f). This phenomenon is not observed at 650 °C. Subsequently, EDS elements mapping was conducted to investigate elements segregation in both grain and annealing twins boundaries.

Figure 8 demonstrates elements distribution in the selected area. No obvious elements segregation could be found along

the annealing twins boundaries, which implies that the annealing twins become unstable and tend to transform into stable grains spontaneously when annealing at 700 °C for longer time. However, significant heterogeneous distribution of elements was observed in grain boundary. One particle enriches in Cr, Ti, Mn and Mo but depletes in Ni, Fe and Co, while the other particle mainly contains more Nb.

#### 4. Discussions

Microstructure evolution of Inconel 625 alloy has been intensively investigated in many studies (Ref 16–19, 21–23). Time–temperature–transformation (TTT) diagram was proposed to predict phase compositions at various temperatures and duration times. There mainly existed three types of carbides in Inconel 625 alloy, including MC,  $M_{23}C_6$ , and  $M_6C$  (Ref 14). Here, MC carbide enriches in Nb and Ti, the  $M_{23}C_6$  carbide contains more Cr, but large amount of Ni, Nb and Mo can be detected in  $M_6C$  carbide. Therefore, MC carbide formed in the Inconel 625 plate as proved by EDS/WDS results in Table 2. Meanwhile, in the sample after annealed at 700 °C for 48 h, carbide enriched in Cr was detected (Fig. 8). Consequently, it is speculated that, except for the dominant MC carbide, a few  $M_{23}C_6$  carbides also formed when annealed at this temperature, which is consistent with the prediction of TTT diagram (Ref 9, 14).



**Fig. 9** TEM images of phase morphology in Inconel 625 alloy after annealed at 700 °C for 48 h: (a) grain boundary, (b–c) inside the grains and (d) annealing twins boundary

Generally,  $\gamma''$  phase precipitates from the matrix at temperatures from 550 to 750 °C. For instance, for as-rolled followed by solution-treated Inconel 625 sheet, formation of  $\gamma''$  phase was observed in the sample after annealing at 650 °C for 10 h (Ref 9). An earlier precipitation of  $\gamma''$  phase at 650 °C was reported in the Inconel 625 alloy as well (Ref 11, 24). In comparison with the results in this study, it can be found that the precipitation of  $\gamma''$  phase was postponed, since this phase is not observed in the foil after 48 h-aging at 650 °C in TEM images (Fig. 7c–d). When the annealing temperature reached 700 °C, a large number of precipitations exist inside the recrystallization grains and along annealing twin boundaries as

shown in Fig. 7. Also based on the TTT diagram (Ref 14), these precipitations should be  $\gamma''$  phase, which is accordance with the TEM observation in Fig. 9. Figure 9 displays the TEM images of phase morphology in different positions. The  $\gamma''$  phase with typical lens morphology linearly distributed along a straight grain boundary as shown in Fig. 9(a). But both irregular lens and near spherical morphologies were found for the precipitated  $\gamma''$  phase inside the recrystallization grains, which further tends to aggregate to form linearly continuous distributed structure as shown in Fig. 9(b–c). The coalescence of  $\gamma''$  particles might indicate the transformation from the metastable  $\text{Ni}_3\text{Nb}$   $\gamma''$  phase into the stable  $\text{Ni}_3\text{Nb}$   $\delta$  phase.

Simultaneously, those particles formed in the annealing twin boundaries mainly have the near spherical morphology in Fig. 9(d). The obtained results confirm previous speculation about the precipitation of  $\gamma''$  phase in Inconel 625 alloy. First precipitated  $\gamma''$  particles were found to be almost spherical, while a progressive morphological change toward a lens morphology was observed as increasing aging duration (Ref 9). Past studies also suggested that  $\gamma''$  phase always nucleates along straight lines that are likely to be sub-grain boundaries, dislocation segments, or twin boundaries (Ref 25), which is in good agreement with the observation in Fig. 9.

Suave et al. have compared the phase transformation of the Inconel 625 alloy in two states (as-rolled + solution-treated, and shear spinning) and observed the slower precipitation of  $\gamma''$  phase in the shear spinning alloy (Ref 9). The precipitation of  $\gamma''$  phase was apparently observed in the shear spinning alloy after annealing at 650 °C for 100 h, but a shorter duration of 10 h at the same temperature led to the formation of this phase in the as-rolled sample. Moreover, the residual strain level affected the secondary carbide stability as well, because a higher content of such carbides was observed in the shear spinning samples after 1000 h at 1173 K (Ref 9). Therefore, the delayed formation of  $\gamma''$  phase in the Inconel 625 foil can be attributed to the severe plastic deformation induced residual plastic strain in the much thinner foil. Here, it should be emphasized that the general phase transformation is not changed in the thinner foil, but the precipitation kinetics could be possibly impacted by the residual stress and/or plastic deformation.

The precipitated  $\gamma''$  phase is regarded as one of the main strengthening phases in the Inconel 625 alloy (Ref 26, 27). However, both the strength and ductility in the foil containing more  $\gamma''$  phase dropped significantly in comparison with the sample after 48 h-aging at 650 °C without this phase as shown in Fig. 5 and Table 3. After carefully comparing the microstructure in Fig. 2 and 3, it is assumed that the worse mechanical properties are attributed to larger recrystallization grain size and coarser carbides. Here, the grain size refinement plays a leading role in the strength since the specimen after annealing at 650 °C for 48 h has small grain size but inversely possesses the best mechanical properties. The past observation in the literature has proven that the cryomilled 625 alloys with smaller grain size showed transcendent mechanical properties than the forged sample (Ref 28). Additionally, much larger and coarser carbides formed as annealing temperature or duration times increased. Carbides appeared in Inconel 625 alloy sometimes inhibit the motion of dislocations as shown in Fig. 7(b), resulting in higher strength. But the coarser carbides serve as predominant stress concentration sites, which cracked or resulted in voids formation at the interface between the carbides and surrounding matrix, and finally, led to the initiation of cracks during deformation (Ref 16, 29). This result further suggests that the Inconel 625 foil is not suitable for long-time usage at the temperature of 700 °C and above.

Another thing should be stressed is the relatively lower elongation of Inconel 625 foil. The tensile elongation of this alloy at room temperature is always over 50%, but that for the foils with various states is below 20%. This might be due to the larger ratio of average grain size to total thickness, while smaller recrystallization grains inducing better ductility as seen in Fig. 2, 3, 4 and 5. Whereas, it is important to emphasize that although the ductility has dropped for the foil, reasonable

values of elongation are still retained as confirmed by fracture surfaces in Fig. 6.

## 5. Conclusions

The Inconel 625 foil with 158 mm in width and 50  $\mu\text{m}$  in height was fabricated through multiple rolling process. After annealing at 650 and 700 °C, the cold-rolled microstructure transformed into smaller recrystallization grain and some annealing twins. Whereas, the fraction and particle size of MC carbides increased with increasing annealing temperature and times. TEM analysis confirms the precipitation of irregular lens and near spherical-shaped  $\gamma''$  phase along the grain boundaries, annealing twins boundaries as well as inside the recrystallization grains at 700 °C, which is not observed in the sample annealed at 650 °C. The foil after annealing at 650 °C for 48 h exhibits the best mechanical properties with UTS and YS of 1515 and 1077 MPa as well as reasonable elongation of 19.5%. The much larger and coarser carbides formed after result in obvious reduction in tensile properties for the sample after 48 h-aging at 700 °C. This result suggests that the Inconel 625 foil is not suitable for long-time usage at the temperature of 700 °C and above.

## Acknowledgments

The authors acknowledge the financial support from the National Key R&D Program of China (No. 2018YFB2003901) and the Science and Technology Major Project of China National Machinery Industry Corporation Ltd. (No. SINOMAST-ZDZX-2019-03). We also thank Mr. Heng Zhang for assistance in EBSD experiments.

## References

1. T. Allen, J. Busby, M. Meyer, and D. Petti, Materials Challenges for Nuclear Systems, *Mater. Today*, 2010, **13**, p 4–23
2. E. Salama, M.M. Eissa, and A.S. Tageldin, Distinct Properties of Tungsten Austenitic Stainless Alloy as A Potential Nuclear Engineering Material, *Nucl. Eng.*, 2019, **51**, p 784–791
3. G.D. Han, Z.P. Lu, X.K. Ru, J.J. Chen, Q. Xiao, and Y.W. Tian, Improving The Oxidation Resistance of 316L Stainless Steel In Simulated Pressurized Water Reactor Primary Water by Electropolishing Treatment, *J. Nucl. Mater.*, 2015, **467**, p 194–204
4. Q.B. He, F.S. Pan, D.Z. Wang, H.D. Liu, F. Guo, Z.W. Wang, and Y.L. Ma, Microstructure and Properties of 316L Stainless Steel Foils for Pressure Sensor of Pressurized Water Reactor, *Nucl. Eng. Tech.*, 2021, **53**, p 172–177
5. C.V. Yıldırım, T. Kıvıkcı, M. Sarıkayac, and Ş Şirin, Evaluation of Tool Wear, Surface Roughness/Topography and Chip Morphology When Machining of Ni-based Alloy 625 under MQL, Cryogenic Cooling and CryoMQL, *J. Mater. Res. Technol.*, 2020, **9**, p 2079–2092
6. Y.B. Gao, Y.T. Ding, J.J. Chen, J.Y. Xu, Y.J. Ma, and X.M. Wang, Effect of Twin Boundaries on The Microstructure and Mechanical Properties of Inconel 625 Alloy, *Mater. Sci. Eng. A*, 2019, **767**, p 702–710
7. K.H. Lo, C.H. Shek, and J.K.L. Lai, Recent Developments in Stainless Steels, *Mater. Sci. Eng. R*, 2009, **65**, p 39–104
8. A.K. Jena and M.C. Chaturvedi, The Role of Alloying Elements in The Design of Nickel- base Superalloys, *J. Mater. Sci.*, 1984, **19**, p 3121–3139
9. L.M. Suave, J. Cormier, P. Villechaise, A. Soula, Z. Hervier, D. Bertheau, and J. Laigo, Microstructural Evolutions During Thermal

- Aging of Alloy 625: Impact of Temperature and Forming Process, *Metall. Mater. Trans. A*, 2014, **45**, p 2963–2982
10. M.D. Mathew, P. Parameswaran, and K.B.S. Rao, Microstructural Changes in Alloy 625 During High Temperature Creep, *Mater. Charact.*, 2008, **59**, p 508–513
  11. F. Cortial, J.M. Corrieu, and C. Vernot-Loier, Influence of Heat Treatments on Microstructure, Mechanical Properties, and Corrosion Resistance of Weld Alloy 625, *Metall. Mater. Trans. A*, 1995, **26**, p 1273–1286
  12. C. Thomas and P. Tait, The Performance of Alloy 625 in Long-term Intermediate Temperature Applications, *Int. J. Press. Vessels Piping*, 1994, **59**, p 41–49
  13. J. Mitra, S. Banerjee, R. Tewari, and G.K. Dey, Fracture Behavior of Alloy 625 with Different Precipitate Microstructures, *Mater. Sci. Eng. A*, 2013, **574**, p 86–93
  14. S. Floreen, G.E. Fuch, W.J. Yang, and E.A. Loria, ed., Superalloys 718, 625, 706 and various derivatives, TMS, Warrendale, 1994, PA, p 13–37
  15. N.D. Evans, P.J. Maziasz, J.P. Shingledecker, and Y. Yamamoto, Microstructure Evolution of Alloy 625 Foil and Sheet During Creep at 750 °C, *Mater. Sci. Eng. A*, 2008, **498**, p 412–420
  16. P. Kontis, A. Kostkaa, D. Raabe, and B. Gault, Influence of Composition and Precipitation Evolution on Damage at Grain Boundaries in A Crept Polycrystalline Ni- based Superalloy, *Acta Mater.*, 2019, **166**, p 158–167
  17. X.D. Liu, J.K. Fan, P.Z. Zhang, J. Xie, F.L. Chen, D.G. Liu, R.H. Yuan, B. Tang, H.C. Kou, and J.S. Li, Temperature Dependence of Deformation Behavior, Microstructure Evolution and Fracture Mechanism of Inconel 625 Superalloy, *J. Alloys Compd.*, 2021, **869**, p 159342
  18. D.F. Li, Q.M. Guo, S.L. Guo, H.J. Peng, and Z.G. Wu, The Microstructure Evolution and Nucleation Mechanisms of Dynamic Recrystallization in Hot-deformed Inconel 625 Superalloy, *Mater. Des.*, 2011, **32**, p 696–705
  19. M.D. Mathew, K.B.S. Rao, and S.L. Mannan, Creep Properties of Service-Exposed Alloy 625 after Resolution Annealing Treatment, *Mater. Sci. Eng. A*, 2004, **372**, p 327–333
  20. S.K. Rai, A. Kumar, V. Shankar, T. Jayakumar, K.B.S. Rao, and B. Raj, Characterization of Microstructures in Inconel 625 Using X-ray Diffraction Peak Broadening and Lattice Parameter Measurements, *Scr. Mater.*, 2004, **51**, p 59–63
  21. M. Sundararaman, L. Kumar, G.E. Prasad, P. Mukhopadhyay, and S. Banerjee, Precipitation of an Intermetallic Phase with Pt<sub>2</sub>Mo-type Structure in Alloy 625, *Metall. Mater. Trans. A*, 1999, **30**, p 41–52
  22. J. Huebner, D. Kata, J. Kusiński, P. Rutkowski, and J. Lis, Microstructure of Laser Cladded Carbide Reinforced Inconel 625 Alloy for Turbine Blade Application, *Ceram. Int.*, 2017, **43**, p 8677–8684
  23. Ö. Özgün, H.Ö. Gülsoy, R. Yilmaz, and F. Findik, Injection Molding of Nickel based 625 Superalloy: Sintering, Heat treatment, Microstructure and Mechanical Properties, *J. Alloys Compd.*, 2013, **546**, p 192–207
  24. L.M. Suave: M.Sc. Dissertation, ISAE-ENSMA, 2012
  25. M. Sundararaman, R. Kishore, and P. Mukhopadhyay, Superalloys 718, 625, 706 and Various Derivatives, E.A. Loria, ed., TMS, Pittsburgh, PA, p 405–417 (1994)
  26. J. Mitra, J.S. Dubey, U.D. Kulkarni, and G.K. Dey, Role of Dislocation Density in Raising the Stage II Work-Hardening Rate of Alloy 625, *Mater. Sci. Eng. A*, 2009, **512**, p 87–91
  27. J. Mitra, J.S. Dubey, and S. Banerjee, Acoustic Emission Technique Used for Detecting Early Stages of Precipitation during Aging of Inconel 625, *Scr. Mater.*, 2003, **49**, p 1209–1214
  28. R. Rodriguez, R.W. Hayes, P.B. Berbon, and E.J. Lavernia, Tensile and Creep Behavior of Cryomilled Inco 625, *Acta Mater.*, 2003, **51**, p 911–929
  29. P. Kontis, D.M. Collins, S. Johansson, A.J. Wilkinson, J.J. Moverare, and R.C. Reed, Crack initiation and propagation during thermal-mechanical fatigue of IN792: effects of dwell time. in *13th International Symposium on Superalloys, SUPERALLOYS 2016*, (pp. 763–772). (2016)

**Publisher's Note** Springer Nature remains neutral with regard to jurisdictional claims in published maps and institutional affiliations.

Springer Nature or its licensor (e.g. a society or other partner) holds exclusive rights to this article under a publishing agreement with the author(s) or other rightsholder(s); author self-archiving of the accepted manuscript version of this article is solely governed by the terms of such publishing agreement and applicable law.